Stochastic Simulation of the Influence of Fibre Path Variability on the Formation of Residual Stress and Shape Distortion

T.S. Mesogitis,[1] A.A. Skordos,[1] A.C. Long[2]
[1]*School of Aerospace, Transport and Manufacturing, Cranfield University, Bedford MK43 0AL, UK*

[2]*Faculty of Engineering, Division of Materials, Mechanics & Structures, University of Nottingham, University Park, Nottingham NG7 2RD, UK*

A stochastic cure simulation approach is developed and implemented to investigate the influence of fibre misalignment on cure. Image analysis is used to characterize fiber misalignment in a carbon non-crimp fabric. It is found that variability in tow orientation is significant with a standard deviation of 1.2°. The autocorrelation structure is modeled using the Ornstein-Uhlenbeck sheet and the stochastic problem is addressed by coupling a finite element model of cure with a Monte Carlo scheme. Simulation of the cure of an angle shaped carbon fiber-epoxy component shows that fiber misalignment can cause considerable variability in the process outcome with a coefficient of variation in maximum residual stress up to approximately 2% (standard deviation of 1 MPa) and qualitative and quantitative variations in final distortion of the cured part with the standard deviation in twist and corner angle reaching values of 0.4° and 0.05° respectively. POLYM. COMPOS., 00:000–000, 2015. © 2015 The Authors Polymer Composites published by Wiley Periodicals, Inc. on behalf of Society of Plastics Engineers

INTRODUCTION

Fiber misalignment is one of the main sources of variability in composites manufacturing. Variability in as supplied dry fabrics and pre-pregs is mainly associated with in-plane and out-of-plane tow waviness setting the minimum level of uncertainty in all subsequent steps of composite manufacturing [1–3]. This uncertainty can affect the forming/draping step introducing significant variability in defect formation [3]. During forming/draping of doubly curved parts the reinforcement is subjected to considerable shear deformation, which may intensify existing geometrical heterogeneities. These phenomena can in turn influence the local fiber volume fraction and porosity distribution, introducing significant variability in permeability [1, 2]. Fiber misalignment with fiber volume fraction variations affect the mechanical, thermo-mechanical and thermal properties of the material during cure and introduce variability in residual stresses and shape distortion. This can affect both the dimensional fidelity of parts and the presence of initial defects such as delaminations and matrix cracks governing mechanical performance.

The issue of variability during the cure step has received limited attention so far in the literature. In particular, the influence of geometrical heterogeneity on the cure process has not been investigated explicitly. A characterization and modeling approach that takes these effects into consideration explicitly is of crucial importance to allow quantification of process outcome variability and its dependence on the level and type of initial variability of the reinforcement. The stochastic simulation framework presented here addresses this aim through the implementation of an image analysis methodology to quantify local fiber angle, the developments of a stochastic object representing fiber angle variability and the integration of these developments with thermomechanical process modeling in a Monte Carlo (MC) scheme. The capabilities of the stochastic simulation scheme are demonstrated using characteristic subcomponent geometry and a variety of lay-ups and the main trends in the sensitivity of residual stress and distortion on fabric variability are uncovered. The overall development addresses the effect of in-plane fiber misalignment and its influence on the process stress developed during the cure process and the associated part distortion.

METHODOLOGY

Image Analysis of Fiber Misalignment of non-Crimp Fabrics

An in-house image analysis code described in detail in [3] developed to characterize fiber misalignment in

Correspondence to: T.S. Mesogitis; e-mail: t.mesogitis@cranfield.ac.uk
Contract grant sponsor: Engineering and Physical Sciences Research Council; contract grant number: EP/IO33513/1; contract grant sponsor: EPSRC Centre for Innovative Manufacturing in Composites (CIMComp).

DOI 10.1002/pc.23856
Published online in Wiley Online Library (wileyonlinelibrary.com).

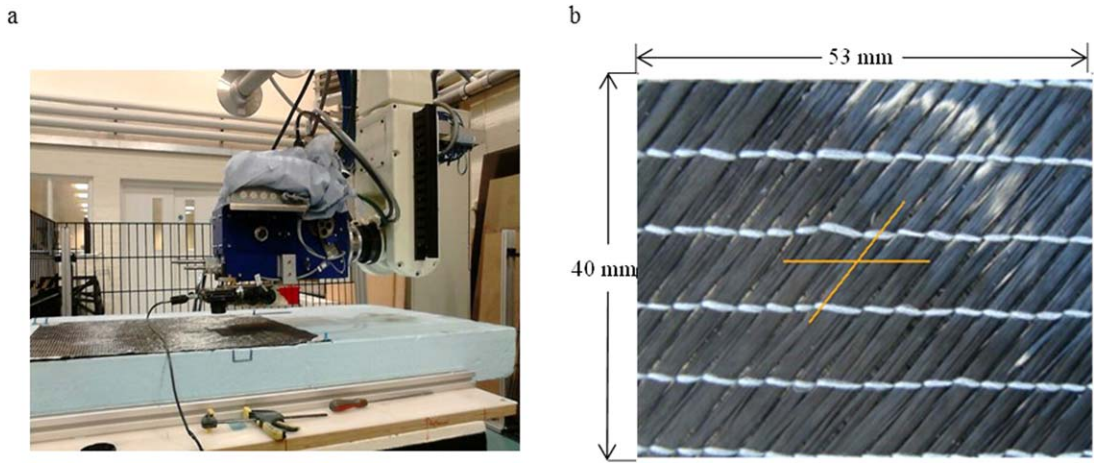

FIG. 1. (a) Experimental set-up, (b) outcome of image analysis of ± 45° NCF. [Color figure can be viewed in the online issue, which is available at wileyonlinelibrary.com.]

woven textiles has been adapted to characterize local variations in unidirectional materials such as non-crimp fabrics (NCF). The image analysis code is based on Fast Fourier Transform (FFT) and correlation analysis. The approach involves calculation of local fiber direction relative to the fiber orientation of a reference image, so that the spatial random field is explicitly quantified. Images are acquired into a discrete pixel array $f(x,y)$. FFT is employed to obtain an approximate estimation of the fiber orientation. Correlation analysis is subsequently used for an accurate calculation of local fiber orientation using a reference region $r_\theta(x,y)$. The analysis is carried out by rotating a kernel $k_\theta(x,y)$ of size $M\times M$ obtained from a reference image. This procedure estimates the tow orientation which maximises the correlation between each image and the reference image. The reference region is:

$$r_\theta(x,\theta)=k_\theta(xcos\theta+ysin\theta,-xsin\theta+ycos\theta) \quad (1)$$

The correlation of a reference region $r_\theta(x,y)$ with the image $f(x,y)$ is:

$$\rho(\theta)=\frac{\sum_{i=1,j=1}^{M,M}\left(r_\theta(x_i,y_i)-\overline{r_\theta}\right)\left(f(x_i,y_i)-\overline{f}\right)}{\sqrt{\sum_{i=1,j=1}^{M,M}\left(r_\theta(x_i,y_i)-\overline{r_\theta}\right)^2\sum_{i=1,j=1}^{M,M}\left(f(x_i,y_i)-\overline{f}\right)^2}} \quad (2)$$

where $\overline{r_\theta}$ and $\overline{f}$ are the averages of $r_\theta(x,y)$ and $f(x,y)$ respectively.

This methodology was applied to images of a 6k carbon fiber ± 45° HTS carbon NCF (Hexcel) with a chain knit stitch pattern and an areal density of 534 g/m^2. A Sony digital camera was mounted on a robotic head (Fig. 1a) in order to control and record the exact position of each image. Seven hundred and forty-eight images were acquired from each side (upper/lower) of the fabric on a 34 × 22 grid with 5 mm spacing. The size of the pixel array was 640 × 480. The image analysis results representing the principal orientation of the image are illustrated as two lines; (i) stitch orientation, (ii) carbon tow orientation (Fig. 1b). The analysis of statistical properties was carried on the full dataset on a 5 × 5 mm grid and additional datasets based on a coarser (10 × 10 mm) and finer (2.5 × 2.5 mm) grid which were produced using the original images. These additional datasets were utilized to verify that the analysis results do not depend on the grid size in terms of variance and autocorrelation structure. In addition, a series of 50 images were acquired at the same location and analyzed to estimate the variance associated with the image acquisition and analysis methodology.

Modeling of the Fiber Orientation Random Field

The random field of fiber angles was modeled using a two-dimensional autoregressive stochastic process, the Ornstein-Uhlenbeck sheet (OU), which is a second order stationary Gaussian process with the following autocovariance function [4, 5]:

$$C(x,y)=\sigma^2 e^{-|x_1-x_2|/b_x-|x_1-x_2|/b_y} \quad (3)$$

Here σ is the standard deviation and b_x and b_y are the correlation lengths in the x and y directions respectively, which determine the decay rate of autocorrelation. Estimation of b_x and b_y was carried out using the generalized reduced gradient non-linear optimization method implemented in Microsoft Excel [6].

To simulate the random field the covariance matrix C is decomposed as a product of its Cholesky root L and its transpose as follows:

$$C=LL^T \quad (4)$$

and the statistical properties of the stochastic process are reproduced by a vector V defined as:

$$V=LY \quad (5)$$

DOI 10.1002/pc

where Y is a vector of independent identically distributed standard normal variables.

Cure Simulation

A coupled thermo-mechanical cure simulation model was implemented in the finite element analysis solver MSC.Marc. The model, which is based on the assumption of Cure Hardening Instantaneously Linear Elastic (CHILE) material [7, 8], was three dimensional and transient. The materials considered were HTS carbon fiber and RTM6 epoxy resin (Hexcel). The material properties depend on both temperature and degree of cure and the material sub-models for cure kinetics, specific heat capacity, thermal conductivity, moduli, cure shrinkage and thermal expansion coefficients were implemented in user defined subroutines UCURE, USPCHT, ANKOND, HOOKLW, USHRINKAGE and ANEXP [9].

The cure kinetics model used in this study is a combination of an nth order model and an autocatalytic model [10], while the specific heat capacity is calculated based on the rule of mixtures. A geometry-based model is applied to compute thermal conductivity [11].

The cure reaction rate is computed as follows [10]:

$$\frac{da}{dt}=k_1(1-a)^{n_1}+k_2(1-a)^{n_2}a^m \tag{6}$$

where a is the degree of cure, k_1, k_2 the reaction rate constants following an Arrhenius law, and m, n_1, n_2 the reaction orders [10].

The composite specific heat capacity is calculated as [12]:

$$c_p=w_f c_{pf}+\left(1-w_f\right)c_{pr} \tag{7}$$

where w_f and c_{pf} is the fiber weight fraction and fiber specific heat capacity, respectively, whereas c_{pr} is the resin specific heat capacity. The specific heat capacity of the fiber is a linear function of temperature whilst the specific heat capacity of the resin depends on both temperature and degree of cure [12].

The thermal conductivity in the fiber direction is the following [11]:

$$K_{11}=v_f K_{lf}+\left(1-v_f\right)K_r \tag{8}$$

where K_{lf} and K_r are the thermal conductivity of the fiber in the longitudinal and transverse direction, respectively. The thermal conductivity in the transverse direction is computed as follows [11]:

$$\begin{aligned}K_{22}=K_{33}=&v_f K_r\left(\frac{K_{tf}}{K_r}-1\right)+K_r\left(\frac{1}{2}-\frac{K_{tf}}{2K_r}\right)\\&+K_r\left(\frac{K_{tf}}{K_r}-1\right)\sqrt{v_f^2-v_f+\frac{\left(\frac{K_{tf}}{K_r}+1\right)^2}{\left(\frac{2K_{tf}}{K_r}-2\right)^2}}\end{aligned} \tag{9}$$

Here K_{tf} is the fiber conductivity in the transverse direction and is a linear function of temperature [13], whilst K_r is the resin thermal conductivity and is dependent on both the degree of cure and temperature [13]. The material sub-models for the cure kinetics (including glass transition temperature development), specific heat capacity and thermal conductivity and the parameters required for these models are presented in detail in [12].

A widely used micro-mechanics model [14] appropriate for unidirectional plies was chosen to model the mechanical properties of the composite as a function of the properties of the constituents. The simplicity of this model as well its direct parametrization in terms of constituent properties makes it a suitable choice for the iterative use required in the context of stochastic simulation. The longitudinal and the transverse moduli are computed as follows:

$$E_{11}=\left(1-v_f\right)E_r+v_f E_{lf} \tag{10}$$

$$E_{22}=\frac{E_r}{1-\sqrt{v_f}\left(1-\frac{E_r}{E_{tf}}\right)}=E_{33} \tag{11}$$

where v_f is the fiber volume fraction, E_r is the isotropic moduli of the resin and E_{lf}, E_{tf} the fiber moduli in the longitudinal and transverse directions respectively. The shear modulus and Poisson's ratio are modeled as follows:

$$G_{12}=\frac{G_r}{1-\sqrt{v_f}\left(1-\frac{G_r}{G_{12f}}\right)}=G_{13} \tag{12}$$

$$v_{12}=v_f\, v_{12f}+\left(1-v_f\right)v_r \tag{13}$$

The mechanical properties of the resin are modeled using a relation that allows a step transition around the instantaneous glass transition temperature:

$$E_r=E_{r_L}+\frac{E_{r_G}-E_{r_L}}{1+e^{C_{rc_p}\left(T-T_g-s\right)}} \tag{14}$$

$$v_r=v_{r_L}+\frac{v_{r_G}-v_{r_L}}{1+e^{C_{rc_p}\left(T-T_g-s\right)}} \tag{15}$$

where T is the current temperature, T_g is the instantaneous glass transition temperature, and C_{rc_p} and s are constants referring to the breadth and temperature shift of the transition around T_g. The values of C_{rc_p} and s are identical to those reported in relation to the specific heat capacity constitutive model for the same epoxy system [10]. Subscripts r_G and r_L denote the material properties of the resin in the glass and liquid/rubber state, respectively.

The longitudinal and transverse cure shrinkage coefficients are modeled as follows:

$$\varepsilon_{11}^S=\frac{\varepsilon_r^S\left(1-v_f\right)E_r}{\left(1-v_f\right)E_r+v_f E_{lf}} \tag{16}$$

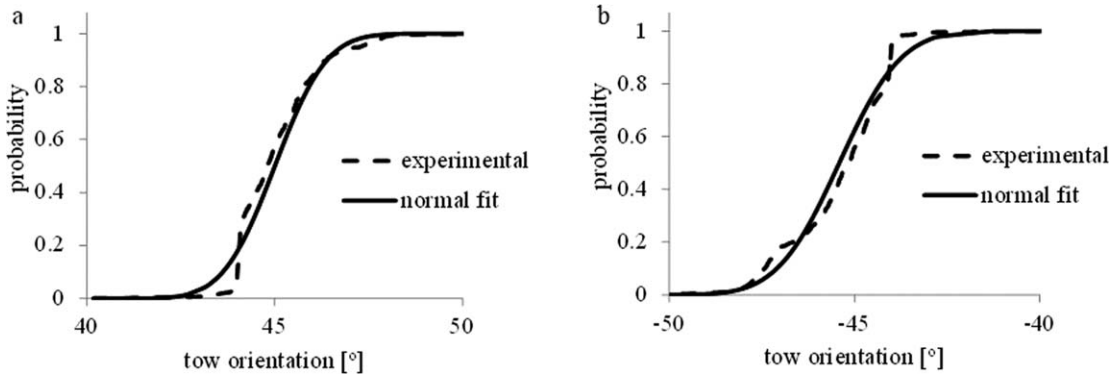

FIG. 2. Statistical behaviour of tow orientation: (a) probability distribution of tow orientation of upper side; (b) probability distribution of tow orientation of lower side.

$$\varepsilon_{22}^{S}=\varepsilon_{r}^{S}\left(\left(v_r+1\right)\left(1-v_f\right)\right)-v_{12}\varepsilon_{11}^{S}=\varepsilon_{33}^{S} \tag{17}$$

where ϵ_r^s is the linear resin cure shrinkage strain which is a function of the resin volumetric cure shrinkage V_r^s:

$$\varepsilon_{r}^{s}=\left(1+V_{r}^{s}\right)^{1/3}-1 \tag{18}$$

The value of V_r^s for the resin of this study is 0.018 [15].

The longitudinal and transverse thermal expansion coefficients are modeled using micromechanics as follows:

$$a_{11}^{th}=\frac{\left(1-v_f\right)E_r a_r+v_f E_{lf} a_{lf}}{\left(1-v_f\right)E_r+v_f E_{lf}} \tag{19}$$

$$a_{22}^{th}=\left(1-v_f\right)a_r+v_f a_{tf}+v_r\left(1-v_f\right)a_r+v_f v_{12f} a_{lf}-v_{12}a_{11}^{th}=a_{33}^{th} \tag{20}$$

where a_r is the resin isotropic thermal expansion coefficient, whilst a_{lf} and a_{tf} are the longitudinal and transverse coefficients of the fiber, respectively. Similarly to the mechanical properties, the resin thermal expansion coefficient follows a step transition around the glass transition using the expression:

$$a_r=a_{r_L}+\frac{a_{r_G}-a_{r_L}}{1+e^{C_{rcp}\left(T-T_g-\sigma\right)}} \tag{21}$$

The fiber thermal expansion coefficients are a polynomial function of temperature and can be computed as [16]:

$$a_{lf}=\sum_{i=0,4}A_{a_{lf}}^{i}T^{i} \tag{22}$$

$$a_{tf}=\sum_{i=0,3}A_{a_{tf}}^{i}T^{i} \tag{23}$$

The mechanical properties of the fiber are presented in [17], whilst the mechanical, thermomechanical and shrinkage parameters of the resin are detailed in [15, 18]. The fiber thermal expansion parameters in *Eqs*. (22 and 23) can be found in [16].

Variability in the cure of a carbon fiber–epoxy subcomponent was modeled by coupling a MC scheme with the finite element cure simulation model. The interface between MC and the cure model was implemented in Fortran. The MC generates realizations of the set of fiber angles over a component using *Eqs*. (3–5), which are input in the finite element model. Once the model solution is complete, the interface reads nodal results and translates to specific metrics relevant to the case studied.

The subcomponent is a 2 mm thick bracket, with two 100 mm long arms. The inner radius of the bracket is 3 mm and its width 40 mm. The standard cure profile for the resin system of this study (160°C cure and 180°C post-cure) was used. Three different lay-up sequences were investigated: a cross-ply $[0/90/90/0]_s$, a bias-ply $[45/-45/-45/45]_s$ and a quasi-isotropic (QI) $[0/45/-45/90]_s$ laminate; here all orientations are with respect to the long axis of the component. The initial temperature was set at 15°C applied to all the nodes of the model. A prescribed temperature boundary condition following the cure profile was applied to the nodes in contact with the tool, whereas natural air convection with a surface heat transfer coefficient of 5 W/(m^2K) was applied on the surface in contact with the vacuum bag.

Incorporation of local tow waviness was carried out by modifying the thermal conductivity matrix, compliance tensor, cure shrinkage coefficient matrix and thermal expansion coefficient matrix. This was performed by applying the coordinate transformation corresponding to the rotation of the principal axis of the individual plies by the angle corresponding to the local fiber misalignment of each element. Enquiries for access to the data referred to in this article should be directed to researchdata@cranfield.ac.uk

RESULTS AND DISCUSSION

Statistical Properties and Spatial Autocorrelation Structure of Fiber *Misalignment*

The image analysis results show that both sides of the fabric present identical statistical behaviour in terms of

 DOI 10.1002/pc

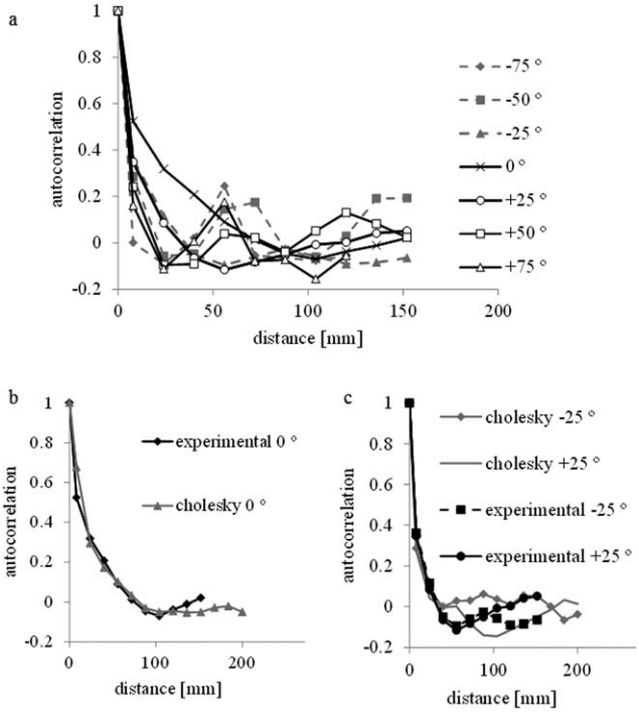

FIG. 3. Directional autocorrelation of tow orientation of ±45° NCF - 0° refers to the orientation of the non-structural stitch; (a) experimental results; (b) simulated tow orientation 0°; (c) simulated tow orientation 25°.

probability distribution and autocorrelation structure. The tow orientation can be represented by a normally distributed variable as shown in Fig. 2. The variability in tow orientation is considerable reaching a standard deviation of 1.2°. The standard deviation obtained for the set of images from a single location is 0.1°, indicating that the experimental and image analysis method introduces negligible variations to the results. No correlation was observed between the tow orientations of the two sides.

Variability comes in patches over the space domain. The autocorrelation structure of the orientation of the tows was investigated in order to study similar behavior of neighboring tows and estimate the spatial dependence of variability. The method of moments was used to quantify spatial autocorrelation between two samples of all pairs of points obtained from the experimental results located at a specific distance and direction as follows:

$$C(x,y)=\sum_{i=1}^{N}\frac{(x_i-\mu)(y_i-\mu)}{N} \tag{24}$$

Here N is the number of observations, x_i and y_i tow orientations at a specific distance and direction and μ the mean value of tow orientation. The spatial autocorrelation of tow orientation as a function of distance and direction is reported in Fig. 3a. The calculation reported in *Eq. 24* was carried out in bins of 25.7° (180°/7) in terms of angle and a distance step of 15 mm with the exception of the first step. In the computational procedure employed the distance and angle between all experimental points against each other are calculated and each pair of points is assigned to the corresponding bin. The distance and angle values used in Fig. 3a correspond to the mid-point of each bin.

It can be observed that fiber misalignment of the ±45° NCF exhibits anisotropic spatial autocorrelation with the major direction of autocorrelation coinciding with the direction of the non-structural stich (0°). This reflects the fact that the majority of variability is introduced during the stitching process of NCF. The autocorrelation in this direction decays towards a negligible plateau value at about 100 mm. In the ±25° directions the autocorrelation reaches a plateau at about 40 mm, whilst autocorrelation at ±50° and ±75° shows a faster decay, reaching zero at approximately 25 mm. The autocorrelation in opposite directions is very similar, suggesting that the autocorrelation structure is quadrant symmetric. The spatial cross-correlation of the orientations in the two sides of the fabric was found to be negligible.

The non-linear fitting applied to the autocorrelation structure yielded a value of 20.2 mm for the autocorrelation length in the direction of the stich (b_x) and 4.7 mm for the length in the normal to the stich direction (b_y). Figures 3b and 3c illustrate the autocorrelation of simulated tow orientation of the NCF used in this study generated on a 68 × 22 grid with 5 mm spacing. It can be observed that the Cholesky factorization reproduces the decay of the autocorrelation structure successfully. There are some discrepancies at the region of the plateau; however this introduces a negligible error as the autocorrelation is close to zero at this region.

Stochastic Simulation of the Propagation of Fiber *Angle Variability Though the Cure Process*

Figure 4 illustrates the final stress in the fiber direction of the outer layers and the final distortion of the component for the deterministic model and one realization of the stochastic simulation for each case. It should be noted that the distortion shown in the deformed shape is multiplied by a factor of 50 to facilitate visualization. Compressive residual stresses are generated in the longitudinal direction whilst tensile residual stresses are generated in the transverse direction, due to the fact that the response of the ply in the longitudinal direction is dominated by the fiber properties and in the transverse direction by the matrix. Shape distortion in the form of spring-in is observed in the case of both the deterministic models and the models incorporating variability in fiber orientation. This is a result of the difference in thermo-mechanical behavior between the out-of-plane and the in-plane directions. In addition to this type of distortion, laminates with stochastic fiber orientation present qualitative differences compared to the nominal cases, as shown in Figure 4. In the case of the cross-ply and quasi-isotropic laminates a twist is present in the realizations of the stochastic model. The twist tends to be more pronounced in the cross ply

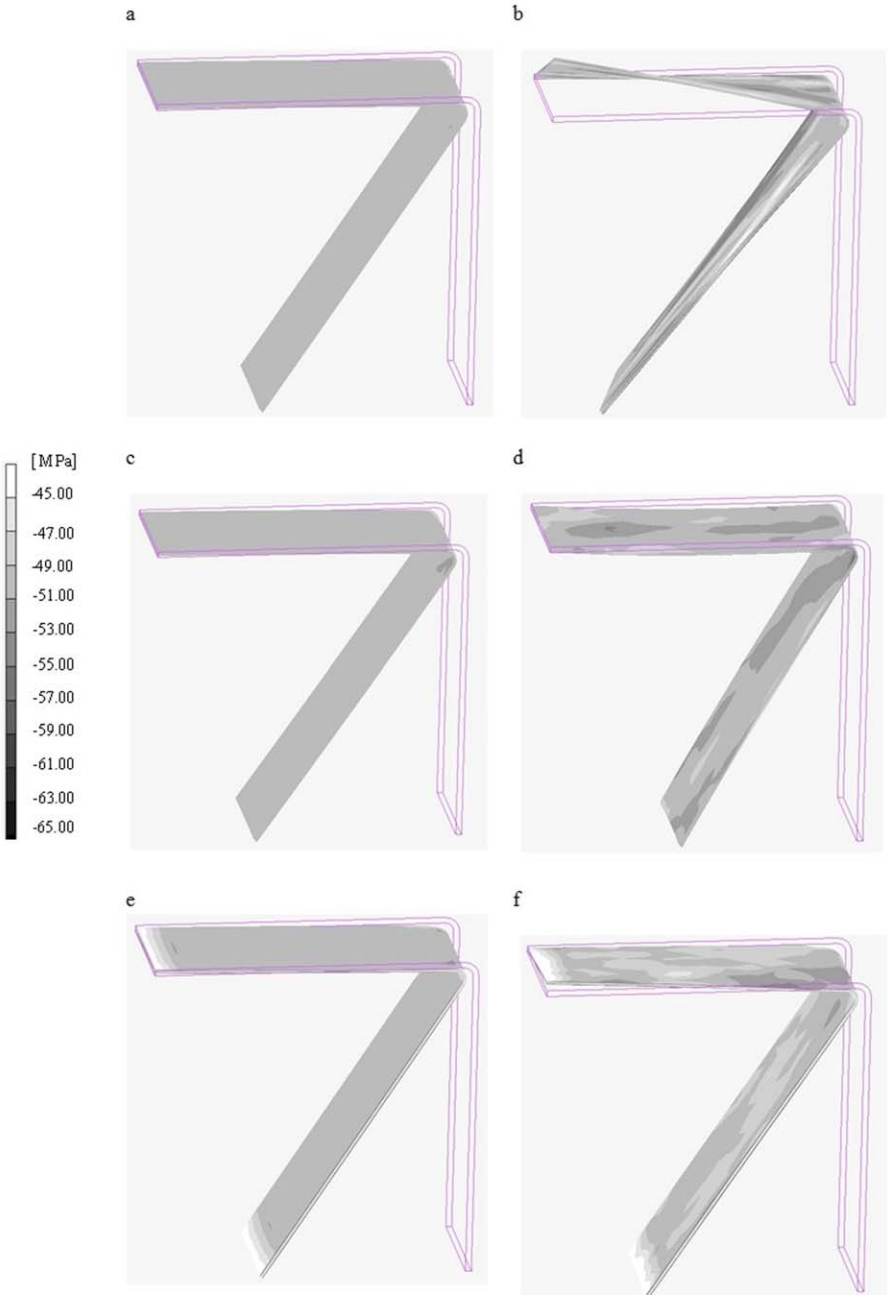

FIG. 4. Residual stress of the outer layers in the fiber direction at the end of the process after release from the tool and final distortion multiplied by a factor of 50: (a) cross ply-deterministic model; (b) cross plystochastic model; (c) bias ply-deterministic model; (d) bias ply-stochastic model; (e) quasi-isotropicdeterministic model; (f) quasi-isotropic-stochastic model. [Color figure can be viewed in the online issue, which is available at wileyonlinelibrary.com.]

than in the quasi-isotropic lay-up. A similar effect occurs in the bias ply laminate, with the qualitative difference that distortion is manifested mainly as bowing of the flange. These effects are due to deviations from the perfect nominal orientations which induce local asymmetry and imbalance in the lay-up. The differences in the type and magnitude of distortion are governed by the differences in stiffness in each lay-up. In the case of the cross ply laminate small variations in fiber angle induce a twisting moment that is not resisted sufficiently by the material, given that no fibers are aligned to the bias direction. As a consequence, twisting becomes the dominant mode of distortion. In contrast, in the case of the bias lay-up twisting is counteracted by the $\pm 45^{\circ}$ layers, whereas any asymmetry induced bending moment is not resisted sufficiently, due to the lack of fibers aligned to the longitudinal direction of the component, resulting in some bowing. The case of the quasi-isotropic laminate is intermediate, with twisting being the dominant mode of distortion due to the fact that the outer layers are 0° and the overall twisting was significantly lower than in the case of the cross ply laminate.

 DOI 10.1002/pc

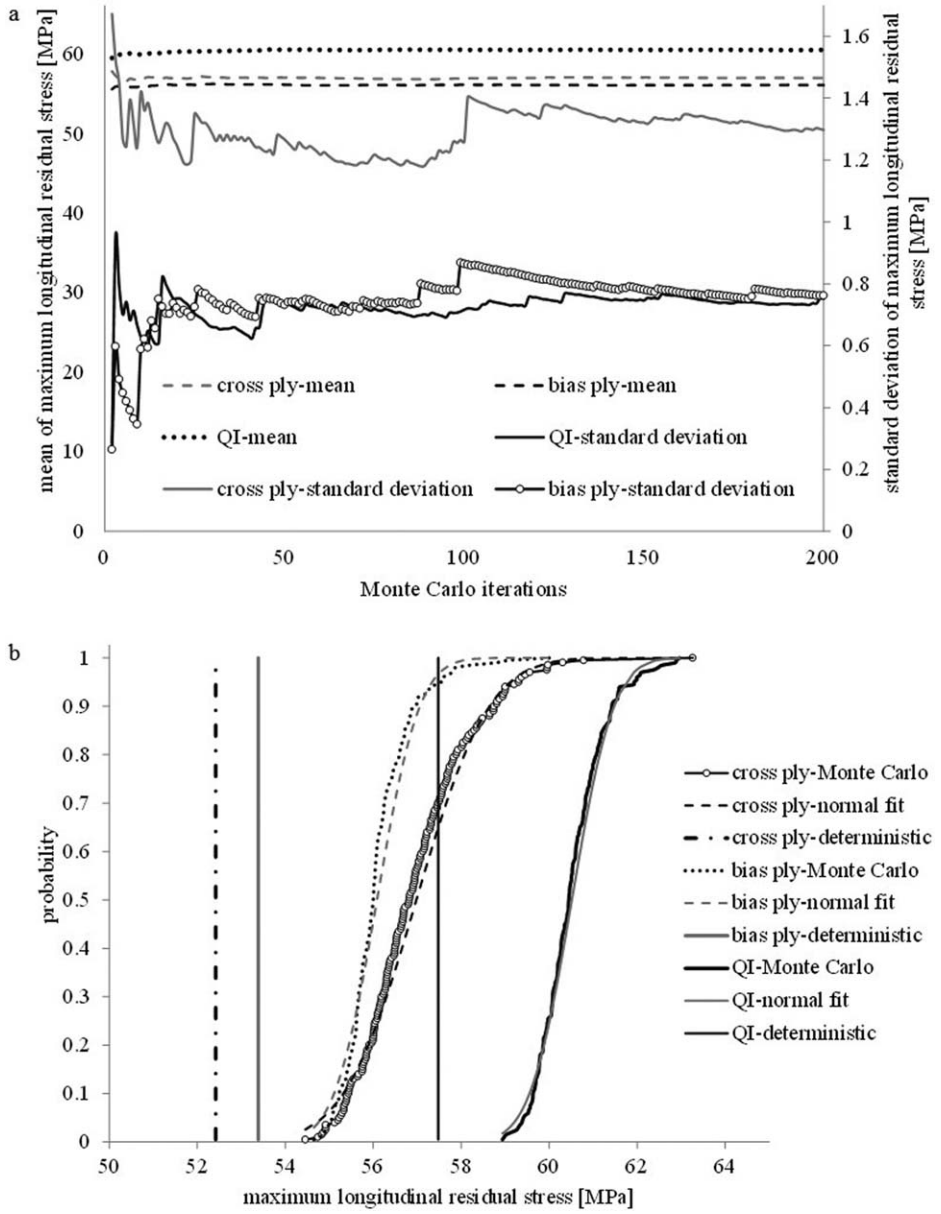

FIG. 5. Convergence of MC simulation: (a) mean and standard deviation of maximum longitudinal residual stress (b) probability distribution of maximum longitudinal residual stress.

Satisfactory convergence was obtained in the MC simulation for the first and second statistical moments of maximum longitudinal residual stress of all layers in the fiber direction after 200 iterations (Fig. 5a). The results suggest that stress presents a coefficient of variation of 2.3, 1.4 and 1.2% (standard deviation of 1.29, 0.76, and 0.75 MPa), for the cross ply, bias ply and quasi-isotropic laminate respectively. Examination of the probability distribution shown in Fig. 5b indicates that maximum stress can be considered a normally distributed random variable. The mean value of stress is higher than the corresponding nominal value resulting from the deterministic simulation in all three case studies, as shown in Fig. 5b. This is due to the fact that the distribution of residual stresses depends on the local properties of the laminate and deviations of the nominal fiber orientation at a local level generate higher levels of stresses locally.

Figures 6a and 6b illustrate the probability distribution of corner distortion of the lower flange, and twist angle of the upper flange of the subcomponent. It should be noted that corner distortion refers to the angle observed at the edge of the lower flange 100 mm distance from the corner and it is a combination of spring-in and bowing effects, whilst twist refers to the angle observed at the edge of the upper flange. The distortion angle exhibits a small variation with a standard deviation not higher than 0.05° for all lay-ups and can be represented by a normally distributed variable. The mean values of both distortion angle and twist converge to values close to the corresponding results from the deterministic simulation for all

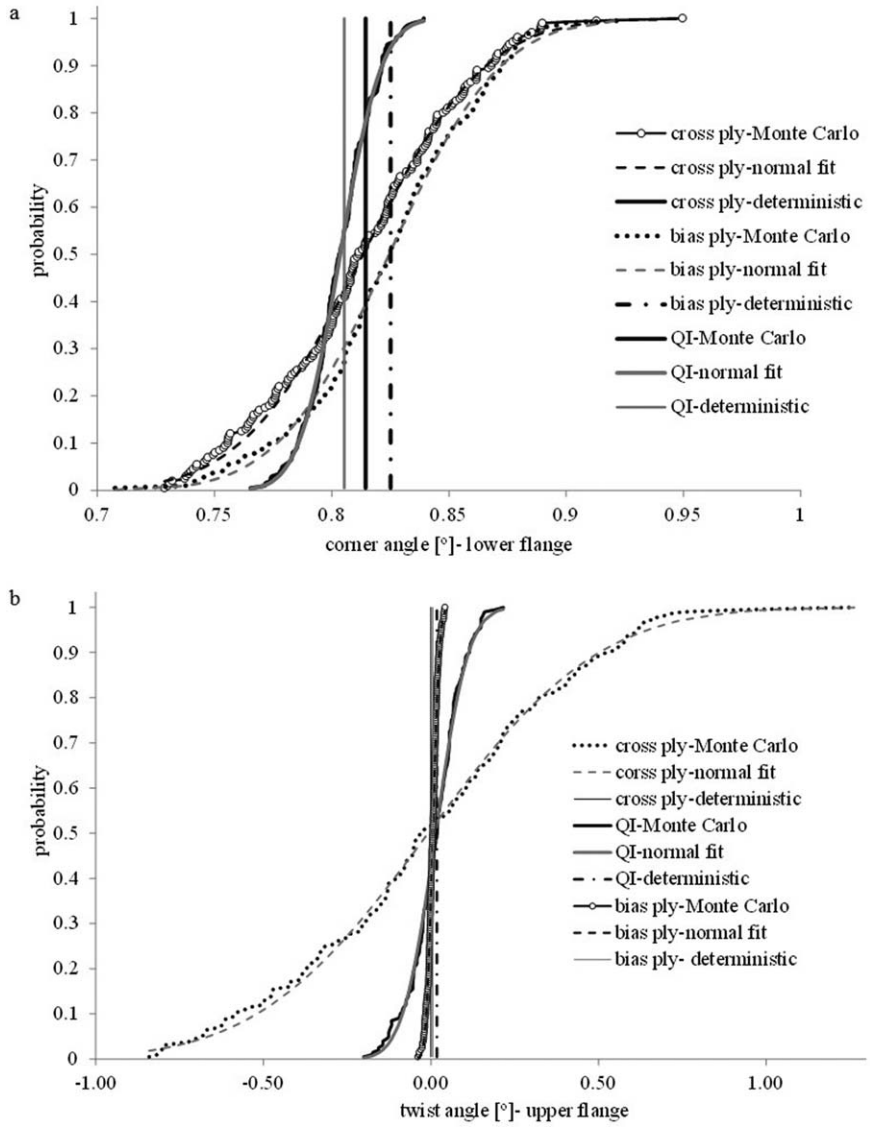

FIG. 6. Shape distortion: (a) probability distribution and deterministic results of corner angle in the lower flange (b) probability distribution and deterministic results of twist angle in the upper flange.

three lay-ups. In addition, small differences exist between the mean values of distortion angle for the different lay-ups. Given that the effective in-plane CTE is the same for the three lay-ups this can be attributed to the presence of twist and bowing. Examination of the deterministic model results illustrated in Fig. 6b suggest that the quasi-isotropic laminate presents a small but finite twist with the bias-ply and cross-ply laminate showing negligible twist. In the case of the deterministic model the perfect cross ply laminate presents no twist due to the fact that no twisting moment is generated. In the case of the perfect bias-ply lay-up twisting is counteracted by the $\pm 45°$ layers, whereas in the case of the perfect quasi-isotropic lay-up the twisting moment is not resisted sufficiently at the bias direction showing the highest levels of twist. This explains the deterministic model results for the maximum longitudinal stress shown in Fig. 5b; higher levels of distortion result in higher stress levels. The twist has a standard deviation of 0.4°, 0.01°, and 0.08°, for the cross ply, bias ply and quasi-isotropic laminate respectively. This is attributed to the differences in stiffness in the bias direction in each lay-up. Therefore, the cross ply laminate is most susceptible to local deviations from the perfect nominal orientations presenting the highest variability in twist given that no fibers are aligned in the $\pm 45°$ directions. In addition, the different levels of variability in twist can explain the differences in standard deviation of maximum stress between the three lay-ups (Fig. 5a). Although for small levels of misalignment the bias ply laminate is expected to show the highest variability in the effective in plane CTE, the quasi-isotropic laminate exhibits the lowest variation in corner angle, whilst the other two lay-ups show higher and similar levels of variability. This is due to the fact that the cross ply and bias ply laminates have high levels of variability in twist and bowing, resulting to higher levels of variability in corner

 DOI 10.1002/pc

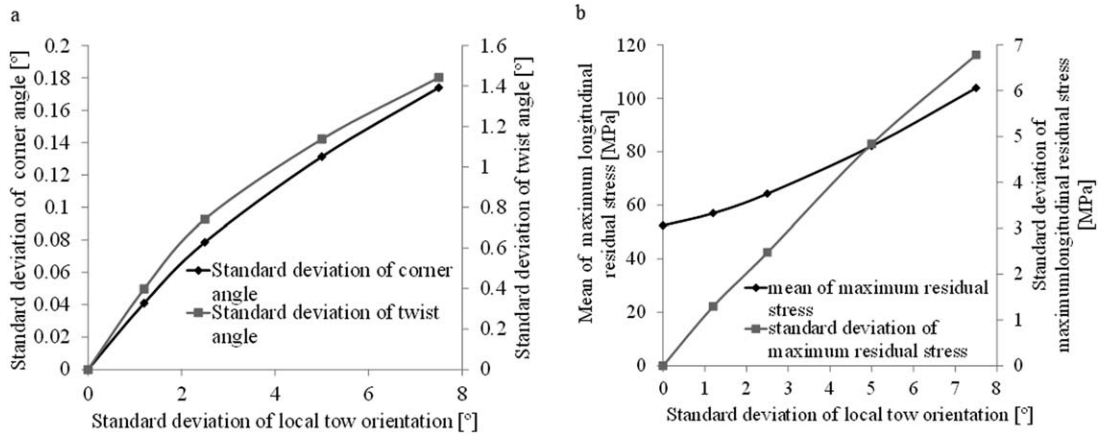

FIG. 7. Sensitivity analysis results, standard deviation: (a) maximum longitudinal stress; (b) shape distortion.

angle, given that the variations are a combination of spring-in, twist and bowing. In the case of the quasi-isotropic laminate the low levels of variability in twist and bowing lead to small variations in corner angle.

The results presented here indicate that fiber misalignment in the order of 1° can introduce significant variability in residual stresses, implying that in the case of higher levels of variability phenomena such as matrix pre-cracking may be affected at a local level. In addition, it is shown that fiber misalignment can considerably alter the final shape of the formed part depending on the lay-up sequence.

Sensitivity of Residual Stress and Distortion to Variance and Autocorrelation Length

Three case scenarios were investigated to study the effect of different levels of variance by setting a standard deviation of 2.5°, 5° and 7.5°, whilst the experimental values of correlation lengths were used in all three cases. In addition, four different case scenarios were studied to investigate the effect of different autocorrelation structure by setting zero correlation lengths, correlation lengths half, double and quadruple the corresponding experimental values, whilst the experimental value of standard deviation was used in all four cases. These results were used alongside the results of the deterministic model and the results of the variability corresponding to the experimental results.

The dependence of output variability on standard deviation of fiber misalignment is illustrated in Figure 7. Both the maximum longitudinal stress average and standard deviation increase with increasing the standard deviation. The mean of maximum residual stress increases due the fact that twist is more pronounced due to higher levels of variability; higher levels of distortion result in higher stresses. The increase of the maximum stress average is non-linear and convex, i.e. the sensitivity of maximum stress on standard deviation of fiber misalignment increases with increasing input variability. This can be explained by the local character of the generation of residual stress, which results in higher maximum stress over the whole component as the probability of extreme local variability increases. The trend of maximum residual stress standard deviation is linear as a function of the standard deviation of tow orientation (Fig. 7a), with a sensitivity of about 1 MPa per 1° of misalignment. This observation points to a generic behavior of a strong dependence of maximum stress and of the likelihood of potential damage on increased variability with the effect being accentuated as variability reaches higher levels. This is combined with a slow decrease in coefficient of variation of the maximum residual stress, indicating that the certainty of the highly non-desirable possibility of damage due to the residual stress increases with increasing variability.

Similarly to residual stresses, increasing the standard deviation in local tow orientation induces an increase of the standard deviation in both corner and twist angle (Fig. 7b). This effect is non-linear following a concave dependence, i.e. the positive sensitivity of both corner and twist angle on the standard deviation of fiber misalignment decreases with increasing variability. This can be explained by the stronger random character of variability as standard deviation increases at the same level of autocorrelation length. Since macroscopic manifestations of variability, such as the twist and corner angle, are affected by the misalignment over an area of the component the increase in random misalignment, whilst global imbalance of the lay-up is kept at the same level, results in a lower sensitivity at higher levels of variability.

Figures 8a and 8b illustrate the effect of correlation lengths. It can be observed that the influence on the mean of maximum residual stress is negligible, whilst the standard deviation of maximum residual stress presents a slight increase as the correlation length increases from zero to the nominal values with a plateau occurring at higher values of correlation lengths (Fig. 8a). This can be attributed

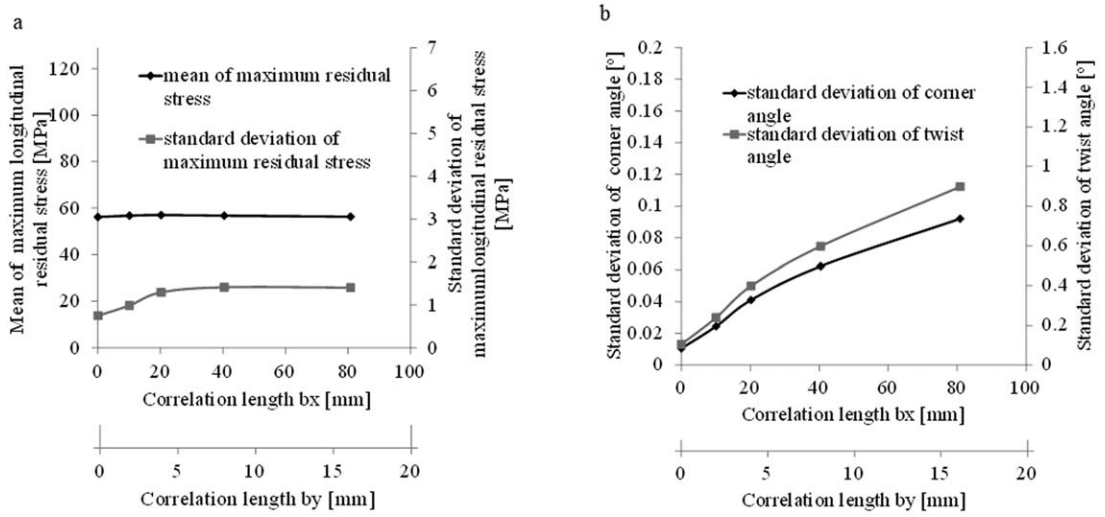

FIG. 8. Sensitivity analysis results, autocorrelation: (a) maximum longitudinal stress; (b) shape distortion.

to the fact that formation of residual stresses is a local phenomenon; therefore it is governed by local tow orientation rather than the dependence of fiber misalignment over the space domain. The slight initial increase in standard deviation of maximum residual stress is caused as tail events are reinforced due to the increased correlation; this influences the standard deviation but not the mean as the effect is symmetric. The effect on standard deviation becomes weaker at high correlation lengths (over 20 mm in the x direction) as the characteristic patches of variability reach a size similar to the width of the component (40 mm).

The standard deviation of both corner and twist angles increases as correlation lengths increase as shown in Fig. 8b. This is attributed to the fact that shape distortion is a macroscopic phenomenon and it increases as imbalances in lay-up introduced by variability increase in size. The dependence is non-linear with a convex curvature at low autocorrelation lengths and a concave curvature at high lengths. The initial increase in sensitivity is due to the stronger effect of macroscopic balances. The sensitivity dependence reverses over 20 mm in the x direction as the size of misaligned areas reached the size of the component.

CONCLUSIONS

The methodologies developed in this work allow the quantification of the influence of variability in fiber orientation on the cure process outcome. The experimental results show that high specification fabrics can involve considerable geometrical variability, which in turn can introduce significant variation to the process outcome. It is found that tow orientation of high specification carbon NCFs can vary with a standard deviation of 1.2°. The stochastic simulation results suggest that maximum residual stress can present a coefficient of variation up to about 2%, whilst the average level of stress is higher than that for the nominal fiber orientations, with potential implications in the performance of manufactured parts. Although the variability in distortion angle is small in absolute terms, considerable qualitative variations in shape can be induced by the presence of fiber geometrical variability. Moreover, shape distortion due to fiber misalignment is significantly dependent on the lay-up, with fiber misalignment having a stronger effect in modes of distortion manifested in the most compliant direction of the component. In addition, the dependence of maximum residual stress and shape distortion on different levels of fiber misalignment and autocorrelation highlight the significance of fiber variability in the development of residual stress during the process and final distortion of the component. These findings are of crucial importance as shape variations lead to considerable part quality and assembly issues, especially in the case of large components.

The modeling approach demonstrated in this study can be extended to characterize and model out of plane fiber misalignment and investigate its influence on heat transfer effects and residual stress formation during the cure process. Furthermore, an integrated framework can be developed and implemented to study the combined effect of different sources of variability such as fiber misalignment, cure kinetics uncertainty and boundary conditions uncertainty, as well as their relative importance on the process outcome. Investigation of quality control data in a production line will allow validation of the stochastic simulation results. This will allow measurement of the statistics in process outcome and will provide the necessary data for comparison with simulation results. The large number or experimental data required implies that his development can be carried out more easily using results on part distortion, rather than stress which would require potentially destructive interventions in manufactured parts.

 DOI 10.1002/pc

In addition, incorporation of variability in process design can minimize the amount of scrap inducing significant benefits in terms of cost and part quality by minimizing variability in process defects such as severe temperature overshoots, residual stresses and shape distortion, and thus, can lead to efficient and robust process designs.

NOMENCLATURE

CHILE	Cure Hardening Instantaneously Linear Elastic
FFT	Fast Fourier Transform
MC	Monte Carlo
NCF	Non-crimp fabrics
OU	Ornstein-Uhlenbeck sheet

REFERENCES

1. B. Verleye, S.V. Lomov, A. Long, I. Verpoest, and D. Roose, *Compos. Part A*, **41**, 1 (2010).
2. A. Endruweit, A.C. Long, F. Robitaille, and C.D. Rudd, *Compos. Part A*, **37**, 1 (2006).
3. A.A. Skordos and M.P.F. Sutcliffe, *Compos. Sci. Technol.*, **68**, 1 (2008).
4. M. Arato, G. Pap, and M.C.A. Van Zuijlen, *Comput. Math. Appl.*, **42**, 1 (2001).
5. G. Terdik and W.A. Woyczynski, *Publ. Math. Debrecen*, **66**, 1 (2005).
6. D. Fylstra, L. Lasdon, J. Watson, and A. Waren, *Interfaces*, **28**, 5 (1998).
7. N. Ersoy, T. Garstka, K. Potter, M.R. Wisnom, D. Porter, and G. Stringer, *Compos. Part A*, **41**, 3 (2010).
8. A. Johnston, R. Vazari, and A. Poursartip, *J. Compos. Mater.*, **35**, 16 (2001).
9. Marc® volume D: User subroutines. Available at: www.mscsoftware.com, (2011).
10. P.I. Karkanas and I.K. Partridge, *J. Appl. Polym. Sci.*, **77**, 7 (2000).
11. J. Farmer and E. Covert, *J. Thermophys. Heat Transfer*, **10**, 3 (1996).
12. T. Mesogitis, A. Skordos, and A. Long, *Compos. Sci. Technol.*, **110** (2015).
13. A.A. Skordos and I.K. Partridge, *Inverse Problems Sci. Eng.*, **12**, 2 (2004).
14. C. Chamis, *J. Compos. Technol. Res.*, **11**, 1 (1989).
15. J. Svanberg, C. Altkvist, and T. Nyman, *J. Reinf. Plast. Compos.*, **24**, 3 (2005).
16. C. Pradere and C. Sauder, *Carbon*, **46**, 14 (2008).
17. T. Vaughan and C. McCarthy, *Compos. Sci. Technol.*, **71**, 3 (2011).
18. Pansart S, Sinapius M, Gabbert U. *Compos. Part A* **40**, 4, (2009).